

# Quantum molecular dynamics simulations for the nonmetal-metal transition in shocked methane

Dafang Li,<sup>1</sup> Ping Zhang,<sup>1,2,\*</sup> and Jun Yan<sup>1,2,†</sup>

<sup>1</sup>*LCP, Institute of Applied Physics and Computational Mathematics,  
Beijing 100088, People's Republic of China*

<sup>2</sup>*Center for Applied Physics and Technology,  
Peking University, Beijing 100871, People's Republic of China*

## Abstract

We have performed quantum molecular-dynamics simulations for methane under shock compressions up to 80 GPa. We obtain good agreement with available experimental data for the principal Hugoniot, derived from the equation of state. A systematic study of the optical conductivity spectra, one-particle density of states, and the distributions of the electronic charge over supercell at Hugoniot points shows that the transition of shocked methane to a metallic state takes place close to the density at which methane dissociates significantly into molecular hydrogen and some long alkane chains. We predict the chemical picture of the shocked methane with respect to the pair correlation function . In contrast to usual assumptions used for high pressure modeling of methane, we find that no diamond-like configurations occurs for the whole density-temperature range studied.

PACS numbers: 65.20.De, 64.30.Jk, 51.70.+f, 31.15.xv

---

\*zhang\_ping@iapcm.ac.cn

†yan\_jun@iapcm.ac.cn

## I. INTRODUCTION

The nature of methane under extreme conditions has recently drawn extensive attentions due to the ongoing scientific and technological interest. As methane is one major constituent of the “ice” layers in Uranus and Neptune, where the pressure ranges between 20 and 600 GPa and temperature between 2000 to 8000 K [1, 2], its properties are of considerable impact on the internal evolution and energetics of these giant planets. The knowledge of its equation of state and electrical conductivity at these conditions are necessary both for theoretical modeling of the composition of these planets and for understanding its contribution to the planetary magnetic fields, which are caused by convective dynamo action of electrically conducting fluid [3]. Thus, it is desirable to determine the transformations in methane induced by nonequilibrium phenomena such as shock waves and detonations.

A lot of efforts have been devoted to exploring the methane chemical dissociation under extreme conditions. At high static pressures between 10 and 50 GPa and temperatures of about 1000 to 3000 K, diamond-anvil cell experiment has suggested that methane breaks down to form diamond and hydrogen [4], in qualitative agreement with Ree’s prediction [5]. However, on the methane Hugoniot [6] different results were reported. No dissociation was found in shocked methane for compressions up to 42 GPa [7], while Nellis et al. observed the increase of electrical conductivity in methane shocked by two-stage light-gas gun, which was attributed to the decomposition into a substantial concentration of molecular hydrogen at 36 GPa and 3900 K [8]. The discrepancy may be caused by the shorter time scale of shock wave experiments. Concerning the theoretical side, empirical potentials [9, 10] and tight-binding simulations [11] have been used to conduct molecular dynamics simulations of the shock compression of methane, while the use of density functional theory in first-principles molecular dynamics simulations [12, 13] provides more accurate modeling of the breaking and forming of chemical bonds. FPMD simulations with 16 methane molecules for 2 picoseconds show that some polymerization reactions occur at 100 GPa and 4000 K and that diamond formation take place only above 300 GPa [12]. Recent ab initio evolutionary simulations [14] have systematically investigated the phase diagram of methane under pressure, and confirmed the dissociation of methane at high pressures. Whereas, the anharmonism was neglected in calculations, which may affects the stability of methane.

To date, although a number of explanatory and predictive results in some cases have al-

ready been provided by experimental and theoretical studies, many fundamental questions of methane at extreme conditions are still much controversial and under debate. The systematic study of equation of state, especially the Hugoniot curve under extreme conditions is far lacking now, which is essential in this context. Furthermore, in adiabatic compressions, the nonmetal-metal transition of hydrocarbons has been a major issue recently. For example, benzene [15] has been reported to transform metallic phase when decomposing into hydrogen under extreme conditions. To date there are still no such data explored for methane, especially due to the difficulties in applying current opacity models at these particular conditions. It is thus highly needed to study the electronic structure, Hugoniot EOS, and optical properties of shocked methane using an efficient method consistently. Quantum molecular dynamics (QMD), where the active electrons are treated in a full quantum mechanical way within the finite temperature density functional theory (FT-DFT), has been proven a successful tool to calculate the properties of complex plasmas under such extreme conditions [16–21]. When combined with the Kubo-Greenwood formulation, the method produces a consistent set of material, electrical, and optical properties from the same simulation and can be applied to various systems.

In the present work, we perform QMD simulations for the system with densities and temperatures ranging from  $0.6 \text{ g/cm}^3$  and 175 K to  $1.5 \text{ g/cm}^3$  and 7000 K along the principal Hugoniot on an intermediate time scale. The analysis of the concentration of molecular species along the Hugoniot based on pair correlation function (PCF) indicates that methane decomposes into molecular hydrogen and saturated hydrocarbons first, and then into long alkane chains at higher pressures and temperatures, which consequently leads to the nonmetal-metal transition. The dynamic conductivity, calculated using the Kubo-Greenwood formula, along with electron density of states and charge distribution, confirms the occurrence of nonmetal-metal transition around 55 GPa. This paper is organized as follows. The simulation details are briefly described in Sec. II; the PCF, which is used to study the dissociation of methane, and Hugoniot curve are given in Sec. III; in Sec IV nonmetal-metal transition, optical properties and electronic properties are discussed. Finally, we close our paper with a summary of our main results.

## II. COMPUTATIONAL METHOD

In the present application, the molecular dynamics trajectories are calculated by employing the Vienna ab initio simulation package (VASP) plane-wave pseudopotential code developed at the Technical University of Vienna [22, 23]. In these simulations, the electrons receive a fully quantum mechanical treatment through solving the Kohn-Sham (KS) equations for a set of orbitals and energies within a plane-wave, FT-DFT formulation [24, 25], where the electronic states are populated according to the Fermi-Dirac distribution at temperature  $T_e$ . The all-electron projector augmented wave (PAW) method [26, 27] is adopted and the exchange-correlation energy is described employing the Perdew-Wang 91 parametrization of the generalized gradient approximation (GGA) [28]. Atoms move classically according to the forces, which originate from the interactions of ions and electrons.

We perform finite-temperature, fixed-volume molecular dynamics simulations for selected densities ranging from 0.6 to 1.5 g/cm<sup>3</sup> and temperatures from 175 to 7000 K that highlight the single-shock Hugoniot region. We use 27 carbon and 108 hydrogen atoms (twenty-seven methane molecules) in a cubic cell and fix the plane-wave cutoff at 600.0 eV which is tested to give good convergence for both total energy and pressure. The Brillouin zone is sampled with the  $\Gamma$  point for molecular dynamics and  $4 \times 4 \times 4$  Monkhorst-Pack [29] scheme  $k$  points for the electronic structure calculations. Integration of the equations of motion proceeds with time steps of 0.5-1.0 fs for different pressure-temperature ranges. Typical simulations run for 8000-16000 steps with the time scale about 8 ps. We let the system equilibrate for 4000-8000 steps and calculate properties using the final 4000-8000 steps. The isokinetic ensemble (NVT) is employed for the ions, where the ion temperature  $T_i$  is fixed using velocity scaling. The electron temperature  $T_e$  is in turn set to that of the ions  $T_i$  based on the assumption of local thermodynamical equilibrium. The accuracy of our calculations is examined by the bond length of CH<sub>4</sub> molecule in its ground state and the result is 1.09, which agrees well with the experiment.

## III. SHOCK EOS AND PCF

A precise description of material properties, such as EOS, is important to the accurate calculation of electrical and optical properties. A crucial measure for theoretical EOS data

is the principal Hugoniot curve. It describes the shock adiabat through a relation between the initial and final internal energy, pressure and volume, respectively,  $(E_0, P_0, V_0)$  and  $(E_1, P_1, V_1)$  according to the following Rankine-Hugoniot equation [30]:

$$(E_1 - E_0) + \frac{1}{2} (V_1 - V_0) (P_0 + P_1) = 0, \quad (1)$$

where the internal energy  $E$  equals to the sum of the ion kinetic energy  $\frac{3}{2}k_B T_i$ , the time average of the DFT potential energy and zero-point energy with  $k_B$  the Boltzmann constant. The pressure consists of contributions from the electronic  $P_e$  and ionic  $P_i$  components, which come from, respectively, the derivatives taken with respect to the KS electronic orbitals and the ideal gas expression since ions move classically. We thus have  $P = P_e + \rho_n k_B T$ , where  $\rho_n$  is the number density. For the methane principal Hugoniot curve, the initial density is  $\rho_0 = 0.423 \text{ g/cm}^3$  and the initial internal energy  $E_0 = 23.30 \text{ eV/molecule}$  at a temperature of 111 K. The initial pressure can be neglected compared to the high pressure of the final state. The Hugoniot points are determined in the following way. For a given density, the periodic crystalline sample of the corresponding size was first constructed. A fixed volume cubic supercell of 27 carbon and 108 hydrogen atoms (27 methane molecules), which is repeated periodically throughout the space, forms the elements of the calculation. A series of quantum molecular dynamics simulations are performed for different temperatures  $T$ . Following it, the internal energies and pressures are determined correspondingly and then fitted to a cubic function of  $T$ . For a given density and a set of temperatures, we plotted  $(V_0 - V_1)(P_0 + P_1)/2$  along with  $(E_1 - E_0)$  as a function of temperature. The intersection of the two curves fixes the principal Hugoniot point  $(E_1, P_1, V_1)$  that satisfies Eq.(1). The particle velocity  $u_p$  and shock velocity  $u_s$  are then determined from the other two Rankine-Hugoniot equations [30],  $V_1 = V_0 [1 - (u_p/u_s)]$  and  $P_1 - P_0 = \rho_0 u_s u_p$ . The principal Hugoniot points of methane derived from Eq. (1) are listed in Table I.

We display our simulated Hugoniot curve for methane in Fig. 1, along with experimental data and results from previous theoretical works. From Fig. 1 we find very good agreement with the experimental results all along the single-shock Hugoniot, while the data from the empirical potential simulations based on the adaptive intermolecular reactive empirical bond order force field presents prominent discrepancy with all the other results, which may be caused by the inaccurate modeling of the breaking and forming of chemical bonds. Our

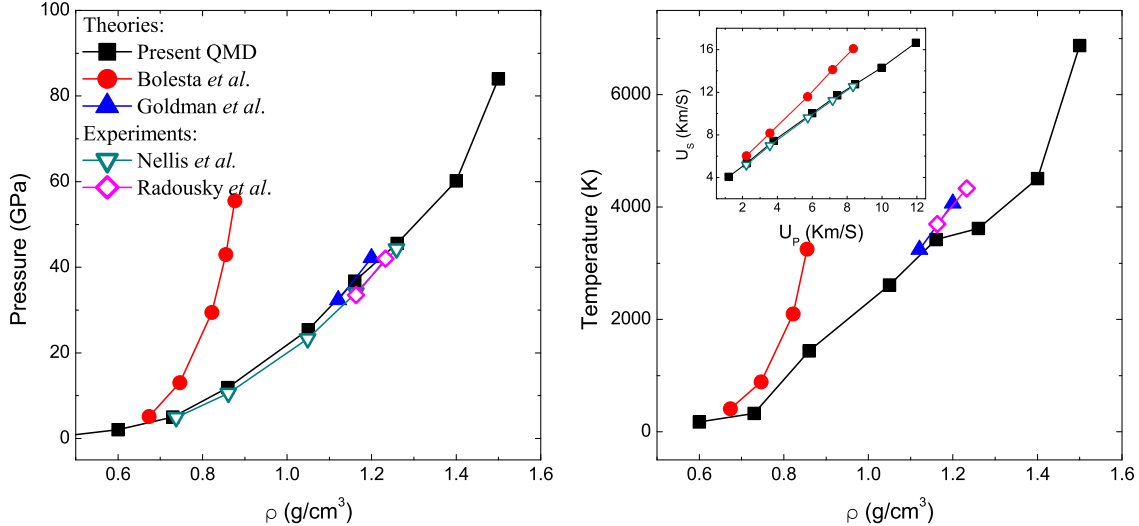


FIG. 1: Principal Hugoniot of methane. For comparison, the present QMD results, together with the previous experimental data (Ref. 6 and Ref. 7) and other theoretical results (Ref. 10 and Ref. 13) are all provided.

simulated pressures and temperatures using QMD show a systematic behavior along the Hugoniot curve, except for the region with a small break in slope of temperature plot between  $1.16$  and  $1.26$  g/cm $^3$ , which usually implies the dissociation of molecular species in the media and thus suggests that methane is dissociating in this density region.

To clarify the structural change in methane under shock conditions, we calculate the PCFs for each pair of atom types, which give the possibility of finding an atom of a given type at a given distance from a reference atom. The PCFs, together with atomic structure along the principal Hugoniot of methane, are presented in Fig. 2. At the lowest density of  $\rho = 0.423$  g/cm $^3$ , the PCF of C-H bond  $g_{\text{C-H}}(r)$  peaks at about 1.09 Å, which corresponds to the equilibrium internuclear distance of the C-H bond in methane molecule. At this density, the hydrogen correlation function does not show a maximum at a distance corresponding to the equilibrium distance of hydrogen molecule  $r_{\text{H-H}} = 0.75$  Å. Meanwhile, no peaks occur in the PCF of C-C bond at 1.50 Å or 1.54 Å, which corresponds to the typical C-C bond length in diamond or saturated hydrocarbons. Therefore, the PCFs at 0.423 g/cm $^3$  indicate that methane remains its ideal molecular configurations without dissociation. As the density is compressed to  $\rho = 1.16$  g/cm $^3$ , methane molecules dissociate with the increase of density and temperature, which is indicated in Fig. 2(b) by the significant reduction and broadening

TABLE I: Points along the principal methane Hugoniot derived from DFT-MD simulations at a series of density ( $\rho$ ), pressure ( $P$ ), and temperature ( $T$ ).

| $\rho$<br>(g/cm <sup>3</sup> ) | $P$<br>(GPa) | $T$<br>(K) |
|--------------------------------|--------------|------------|
| 0.60                           | 2.06         | 176        |
| 0.73                           | 5.02         | 330        |
| 0.86                           | 11.89        | 1441       |
| 1.05                           | 25.42        | 2614       |
| 1.16                           | 36.74        | 3420       |
| 1.26                           | 45.55        | 3620       |
| 1.40                           | 60.20        | 4509       |
| 1.50                           | 84.00        | 6875       |

of the maxima of  $g_{\text{C-H}}(r)$  around 1.09Å. On the other hand, the  $g_{\text{H-H}}$  and  $g_{\text{C-C}}$  PCFs at this density indicate that small amount of hydrogen and saturated hydrocarbons form molecules upon dissociation of methane. Consistently, the atomic configuration consists of a mixture of methane and ethane with the residual hydrogen atoms both in molecular and atomic forms as shown in the inset of Fig. 2(b). As the density is further increased to 1.26 g/cm<sup>3</sup>, maximum of the PCF  $g_{\text{C-H}}(r)$  continues to reduce and broaden while the peaks of  $g_{\text{H-H}}(r)$  and  $g_{\text{C-C}}(r)$  increase, which indicates that methane further dissociates into hydrogen and some hydrocarbons of higher molecular weight. This trend persists up to a density of 1.4 g/cm<sup>3</sup>, except that a new species of long alkane chains show up in the atomic configuration. It is indicative of the formation of C-C bonds favored with increasing density, though still no diamond-like carbons form in the density range considered here, in agreement with earlier predictions.

#### IV. DYNAMIC OPTICAL AND ELECTRONIC PROPERTIES

Following the QMD simulations, a total number of 10 to 15 configurations are selected from an equilibrated (in an average sense) portion of the molecular dynamics run, typically

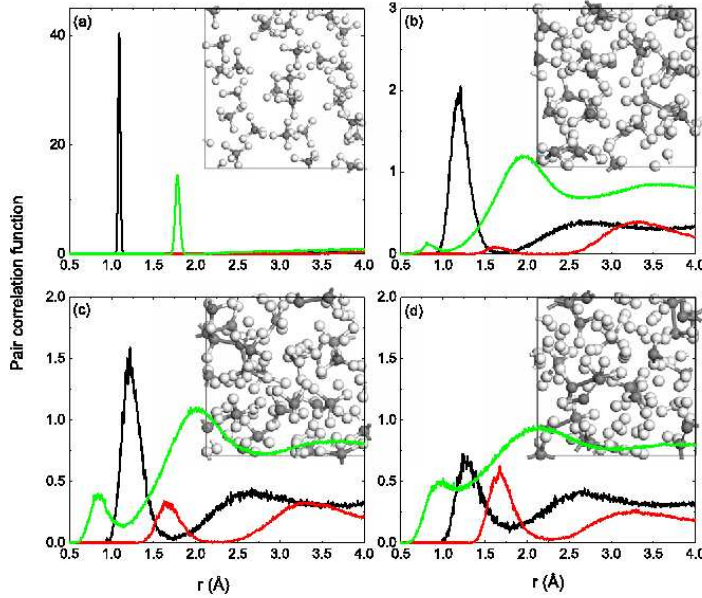


FIG. 2: Pair-correlation functions for C-C (red or gray line), C-H (black line), H-H (green or light gray line) along the principal methane Hugoniot. The atomic structure, where carbon and hydrogen atoms are denoted by gray and white balls, respectively, is also provided in the insets. (a) $\rho = 0.423 \text{ g/cm}^3$ ,  $T = 111 \text{ K}$ ; (b) $\rho = 1.16 \text{ g/cm}^3$ ,  $T = 3420 \text{ K}$ ; (c) $\rho = 1.26 \text{ g/cm}^3$ ,  $T = 3620 \text{ K}$ ; (d) $\rho = 1.40 \text{ g/cm}^3$ ,  $T = 4509 \text{ K}$ .

sampling the final picosecond of evolution. The configurations are spaced at time steps separated by at least the correlation time, the  $e$ -folding time of the velocity autocorrelation function. The calculated properties should be averaged over the number of representative configurations or snapshots employed. For each of these configurations, the electrical conductivity is calculated using the most general formulation given by the Kubo-Greenwood formulation, without particular assumptions made on the ionic structure or on the electron-ion interactions. In the framework of the quasi-independent particle approximation, the Kubo-Greenwood formulation [31, 32] gives the real part of the electrical conductivity as a function of frequency  $\omega$ ,

$$\begin{aligned} \sigma_1(\omega) = & \frac{2\pi}{3\omega\Omega} \sum_{\mathbf{k}} w(\mathbf{k}) \sum_{j=1}^N \sum_{i=1}^N \sum_{\alpha=1}^3 [f(\epsilon_i, \mathbf{k}) - f(\epsilon_j, \mathbf{k})] \\ & \times |\langle \Psi_{j,\mathbf{k}} | \nabla_\alpha | \Psi_{i,\mathbf{k}} \rangle|^2 \delta(\epsilon_{j,\mathbf{k}} - \epsilon_{i,\mathbf{k}} - \hbar\omega), \end{aligned} \quad (2)$$

where  $\omega$  is the frequency,  $\Omega$  is the volume of the supercell,  $N$  is the total number of energy bands used,  $\Psi_{i,\mathbf{k}}$  and  $\epsilon_{i,\mathbf{k}}$  are the electronic eigenstates and eigenvalues for the electronic state  $i$  at  $\mathbf{k}$ ,  $f(\epsilon_i, \mathbf{k})$  stands for the Fermi distribution function, and  $w(\mathbf{k})$  represents the  $\mathbf{k}$ -point weighting factor. Other properties can be directly derived from the frequency-dependent real part of the electrical conductivity. An application of the Kramer-Krönig relation yields the imaginary part  $\sigma_2(\omega)$  as

$$\sigma_2(\omega) = -\frac{2}{\pi}P \int \frac{\sigma_1(\nu)\omega}{(\nu^2 - \omega^2)} d\nu, \quad (3)$$

where  $P$  stands for the principal value of the integral. The real and imaginary parts of dielectric function, in turn, follow immediately from the electrical conductivity as

$$\epsilon_1(\omega) = 1 - \frac{4\pi}{\omega}\sigma_2(\omega), \quad (4)$$

$$\epsilon_2(\omega) = \frac{4\pi}{\omega}\sigma_1(\omega). \quad (5)$$

And then the real  $n(\omega)$  and imaginary  $k(\omega)$  parts of the optical refraction index have relation with the dielectric function by a simple formula,

$$\epsilon(\omega) = \epsilon_1(\omega) + i\epsilon_2(\omega) = [n(\omega) + ik(\omega)]^2. \quad (6)$$

Finally, the reflectivity  $r(\omega)$  and absorption coefficient  $\alpha(\omega)$  can be determined from these quantities,

$$r(\omega) = \frac{[1 - n(\omega)]^2 + k(\omega)^2}{[1 + n(\omega)]^2 + k(\omega)^2}, \quad (7)$$

$$\alpha(\omega) = \frac{4\pi}{n(\omega)c}\sigma_1(\omega). \quad (8)$$

In Fig. 3 the behavior of the frequency-dependent conductivity  $\sigma_1(\omega)$  at different Hugo-niot points is reported in “raw” data form. It is found that  $\sigma_1(\omega)$  at these four different

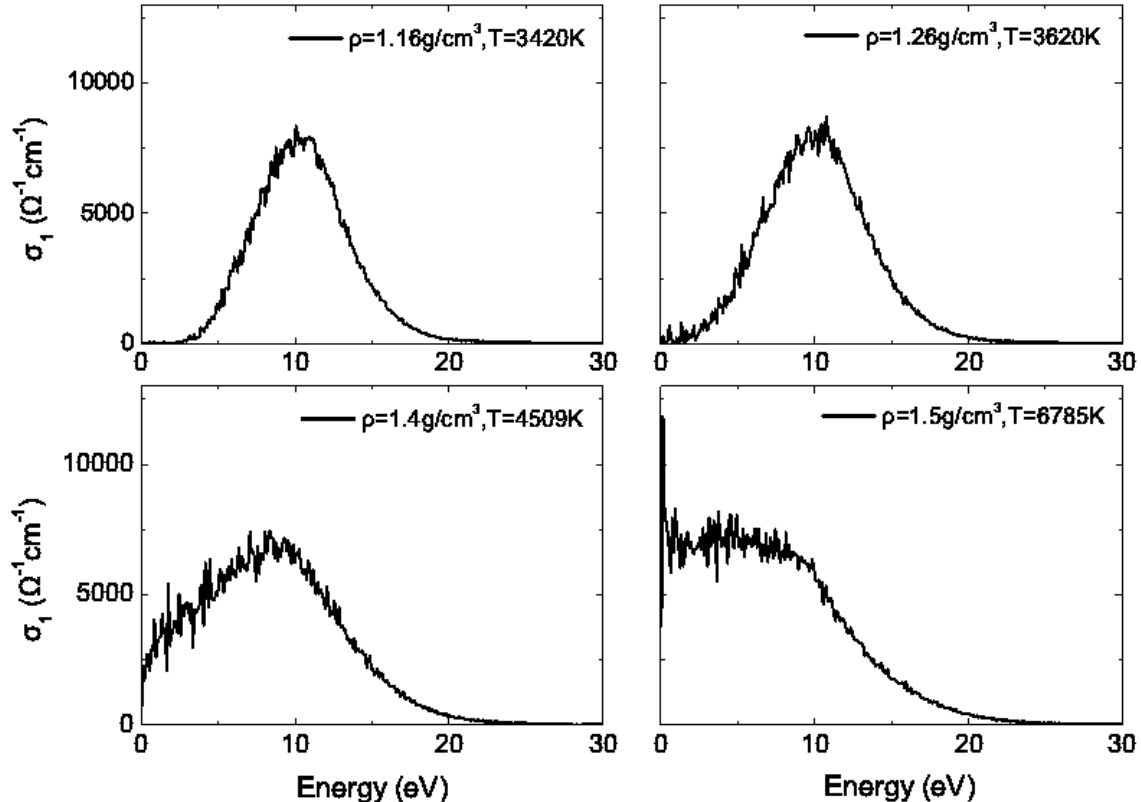


FIG. 3: The real part of the dynamic electrical conductivity along the principal Hugoniot. Data have been averaged over 10 to 15 uncorrelated MD configurations.

densities exhibit a uniform feature that they peak around 10.0 eV, which can be associated with transitions to the lowest excited states, and vanish above 25.0 eV. With the increase of density and temperature along the principal Hugoniot, the shape of  $\sigma_1(\omega)$  mostly keeps the same, but the main peak moves to lower frequencies, which consequently leads to a significant increase in dc conductivity, given as  $\sigma_{dc} = \lim_{\omega \rightarrow 0} \sigma_1(\omega)$ . This significant change of the dc conductivity along principal Hugoniot is displayed in Fig. 4. For comparison, the experimental data is also included. The difference between our calculated results and the experimental results may come from the under-prediction of the Hugoniot temperatures for methane by quantum molecular dynamics. The dc conductivity is negligible for pressures up to 40 GPa, where methane exhibits insulating behavior. Then, it increases to 128  $\Omega^{-1}\text{cm}^{-1}$  for pressures between 40 and 50 GPa. For pressures above 55 GPa, the dc conductivity increases to a value larger than 1000  $\Omega^{-1}\text{cm}^{-1}$ . A decisive physical assertion to define the metallicity of such disordered system has been proposed by Ioffe et al. and developed by Mott [33, 34], which states that any high-temperature, disordered system will remain

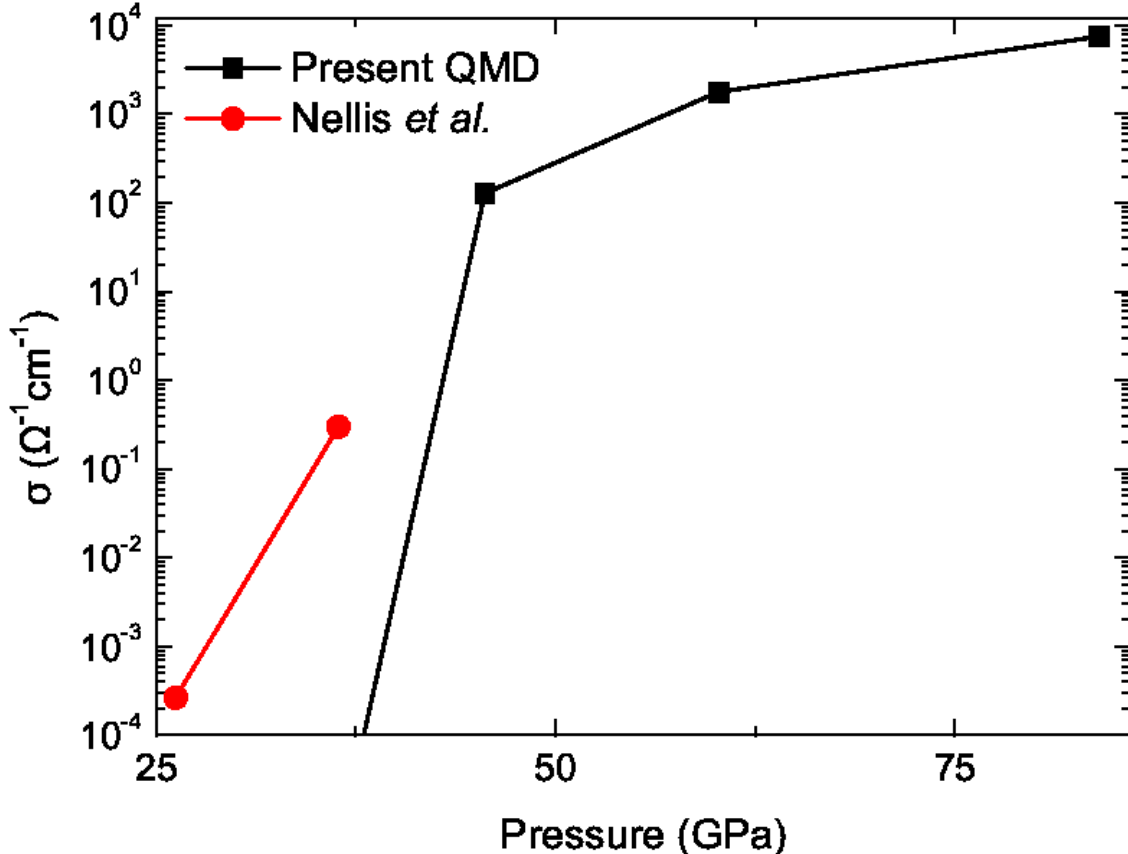


FIG. 4: The dc conductivity of our results and data from Ref. 8 are plotted along the principal Hugoniot.

metallic or indeed attain metallic status if the characteristic mean free path of the valence electrons exceeds the mean distance between the constituent atoms or molecules providing those carriers of electrical current. This simple but powerful argument leads to an estimate of the minimum metallic conductivity of about  $2000 \Omega^{-1} \text{cm}^{-1}$  for fluid hydrogen, rubidium, caesium and mercury, whereby transitions from non-metallic to metallic fluids have recently been observed in the nominally non-metallic chemical elements hydrogen, oxygen and nitrogen at high pressures and temperatures [35, 36]. With the similar minimum metallic conductivity for fluid methane, it is indicated that nonmetal-metal transition takes place in shocked methane. This nonmetal-metal transition clearly suggests that the dissociation of the molecular fluid along the Hugoniot has major consequences to the electrical conductivity of the system. Interestingly, such nonmetal-metal transition in fluid hydrogen occurs under similar conditions [37, 38].

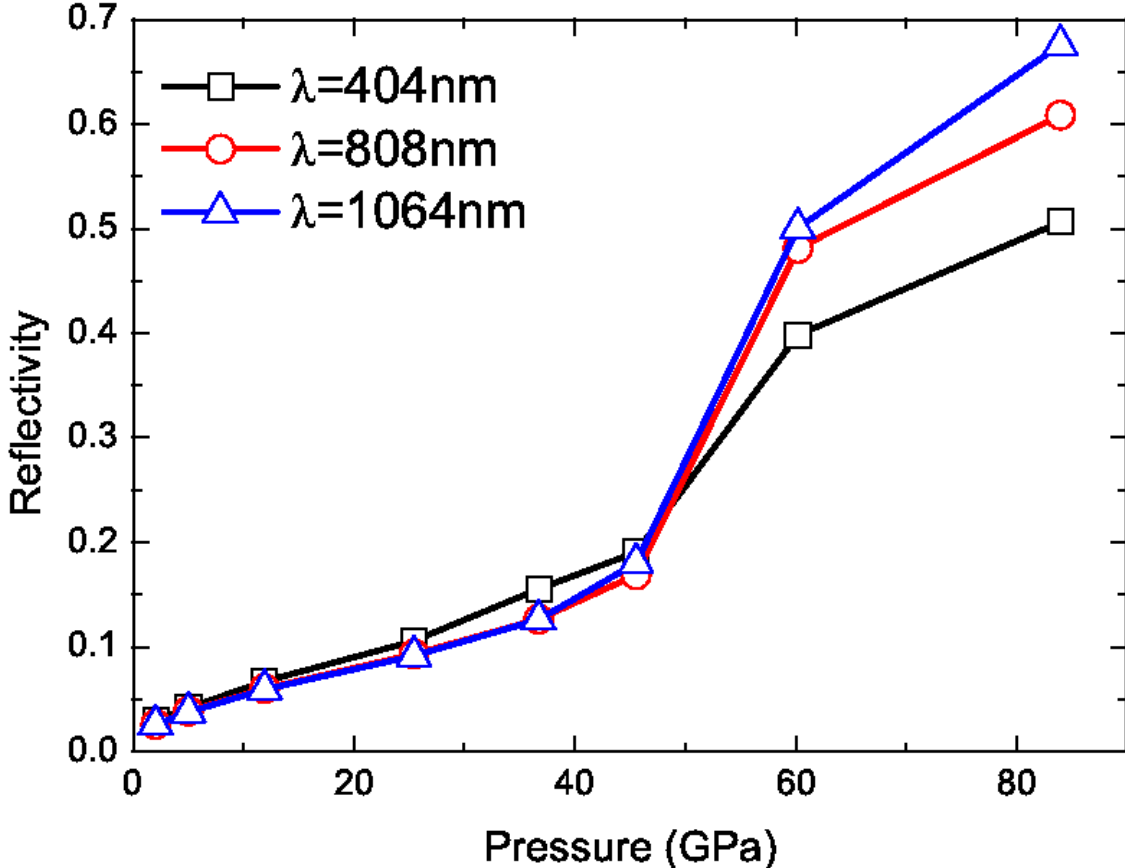


FIG. 5: Optical reflectivity of shocked methane for wavelengths of 404 (black square), 808 (red circle) and 1064 nm (blue triangle) along the Hugoniot.

As the optical reflectivity of fluid has been successfully probed in dynamic compression experiments [39], we show in Fig. 5 the reflectivity  $r(\omega)$  at typical wavelengths of 404, 808 and 1064 nm spanning the visible spectrum. It can be seen that a measurable reflectivity arises from 0.05 to 0.35-0.68 for the principal shocks, which is related with the high-pressure nonmetal-metal transition. For pressures between 25 and 45 GPa reflectivity increases monotonically and is essentially equal for all three frequencies, while around 55 GPa the increase becomes sharper due to the nonmetal-metal transition, after which the increase slows down.

Furthermore, we examine the variation of the electron density of states (EDOS) along the Hugoniot to clarify the origin of this nonmetal-metal transition. Still use the selected ten to fifteen configurations used in the above optical properties calculations, we calculate the electron density of states. Each of these configurations repeats periodically throughout the space and forms the elements of the calculation. In Fig. 6 the averaged EDOS is presented

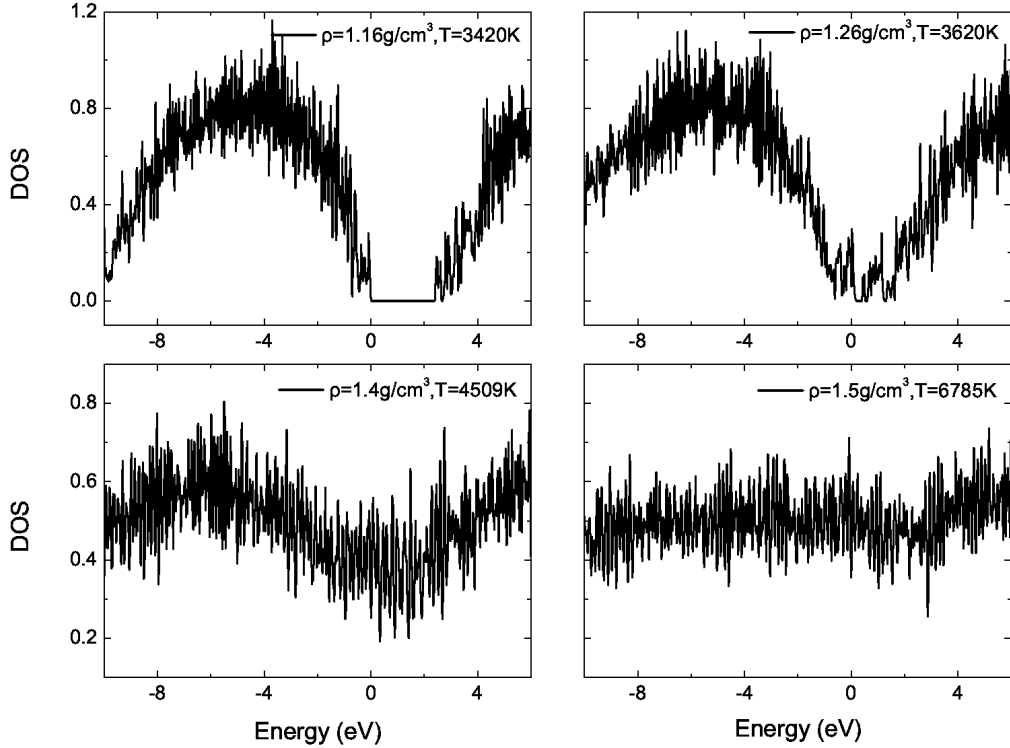


FIG. 6: Electronic density of states of liquid methane along the principal Hugoniot: (a) $\rho = 1.05 \text{ g/cm}^3$ ,  $T = 2614 \text{ K}$ ; (b) $\rho = 1.16 \text{ g/cm}^3$ ,  $T = 3420 \text{ K}$ ; (c) $\rho = 1.26 \text{ g/cm}^3$ ,  $T = 3620 \text{ K}$ ; (d) $\rho = 1.40 \text{ g/cm}^3$ ,  $T = 4509 \text{ K}$ . Data have been averaged over 10 to 15 uncorrelated MD configurations. The zero of the energy scale shows the position of the Fermi level.

for different Hugoniot points. As can be seen, at  $\rho = 1.16 \text{ g/cm}^3$  and  $T = 3420 \text{ K}$ , EDOS clearly exhibits a gap around 2.4 eV, where only thermally activated electron transport occurs as in semiconductors. With the density and temperature increasing, the band gap is reduced gradually and closed eventually. And thus a higher, metal-like conductivity follows.

Another way to characterize this behavior is the change of the charge density with increasing density as shown in Fig. 7, from which it is clearly seen that a transition from a disconnected network (left panel) to a connected one (right) occurs as density increases. This suggests that the electrons are still localized for the lower density, while transient filaments and lusters form as percolating path for the higher density, which leads to a metal-like behavior.

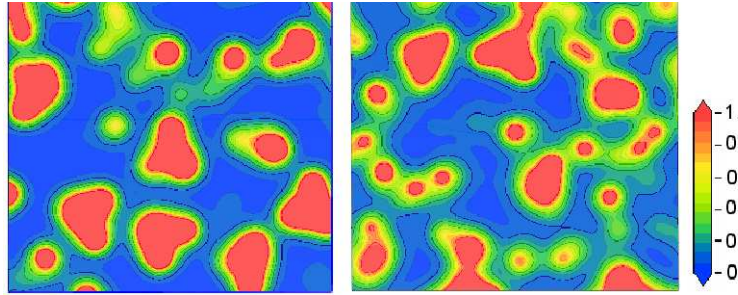


FIG. 7: Typical contour plots of the charge densities in units of  $e/\text{\AA}^3$  for  $0.86 \text{ g}/\text{cm}^3$  at  $1441 \text{ K}$  (left panel) and  $1.4 \text{ g}/\text{cm}^3$  at  $4509 \text{ K}$  (right panel) along a slice through the simulation box.

## V. CONCLUSIONS

In summary, through systematic QMD simulations we have determined the shocked EOS and clarified the high-pressure nonmetal-metal transition of the fluid methane. The increase of electrical conductivity with pressure can be ascribed to the dissociation of the molecular fluid. However, no diamond-like carbon forms in the density range considered here. In addition, the optical properties of warm dense methane are also calculated, from which an experimentally measurable increase in the reflectivity associated with the high-pressure nonmetal-metal transition has been found. It is expected that our simulated results of shocked methane would have a strong influence on models for planetary interiors.

### Acknowledgments

This work was supported by NSFC under Grant No. 51071032 and 10734140, and by the National Fundamental Security Research Program of China.

- [1] W. B. Hubbard, and J. M. MacFarlane, *J. Geophys. Res.* **85**, 225 (1980).
- [2] D. J. Stevenson, *Annu. Rev. Earth Plane Sci.* **14**, 257 (1982).
- [3] D. J. Stevenson, *Rep. Prog. Phys.* **46**, 555 (1983).
- [4] L. R. Benedetti, J. H. Nguyen, W. A. Caldwell, H. J. Liu, M. Kruger, R. Jeanloz, *Science* **286**, 100 (1999).
- [5] F. H. Ree, *J. Chem. Phys.* **70**, 974 (1979).

- [6] W. J. Nellis, F. H. Ree, M. van Thiel, and A. C. Mitchell, *J. Chem. Phys.* **75**, 3055 (1981).
- [7] H. B. Radousky, A. C. Mitchell, and W. J. Nellis, *J. Chem. Phys.* **93**, 8235 (1990).
- [8] W. J. Nellis, D. C. Hamilton, and A. C. Mitchell, *J. Chem. Phys.* **115**, 1015 (2001).
- [9] M. L. Elert, S. V. Zybin and C. T. White, *J. Chem. Phys.* **118**, 9795 (2003).
- [10] A. V. Bolesta, L. Q. Zheng, D. L. Thompson, and T. D. Sewell, *Phys. Rev. B* **76**, 224108 (2007).
- [11] J. D. Kress, S. R. Bickham, L. A. Collins, B. L. Holian, and S. Goedecker, *Phys. Rev. Lett.* **83**, 3896 (1999).
- [12] F. Ancilotto, G. L. Chiarotti, S. Scandolo, and E. Tosatti, *Science* **275**, 1288 (1997).
- [13] N. Goldman, E. J. Reed, and L. E. Fried, *J. Chem. Phys.* **131**, 204103 (2009).
- [14] G. Y. Gao, A. R. Oganov, Y. M. Ma, H. Wang, P. F. Li, *J. Chem. Phys.* **133**, 144508 (2010).
- [15] C. Wang, and P. Zhang, *J. Appl. Phys.* **107**, 083502 (2010).
- [16] L. Collins, S. Bickham, J. Kress, S. Mazeved, T. Lenosky, and W. Windl, *Phys. Rev. B* **63**, 184110 (2001).
- [17] S. Mazeved, L. Collins, N. Magee, J. Kress, and J. Keady, *Astron. Astrophys.* **405**, L5 (2003).
- [18] J. Kress, S. Mazeved, L. Collins, and W. Wood, *Phys. Rev. B* **63**, 024203 (2001).
- [19] M. P. Desjarlais, J. D. Kress, and L. A. Collins, *Phys. Rev. E* **66**, 025401 (2002).
- [20] S. Mazeved, P. Blottiau, J. D. Kress, and L. A. Collins, *Phys. Rev. B* **69**, 224207 (2004).
- [21] Y. Laudernet, J. Clerouin, and S. Mazeved, *Phys. Rev. B* **70**, 165108 (2004).
- [22] G. Kresse, and J. Hafner, *Phys. Rev. B* **47**, 558 (1993).
- [23] G. Kresse, and J. Furthmüller, *Phys. Rev. B* **54**, 11169 (1996).
- [24] T. Lenosky, S. Bickham, J. Kress, and L. Collins, *Phys. Rev. B* **61**, 1 (2000).
- [25] S. Bagnier, P. Blottiau, and J. Clerouin, *Phys. Rev. E* **63**, 015301(R) (2001).
- [26] G. Kresse, and J. Joubert, *Phys. Rev. B* **59**, 1758 (1999).
- [27] P. E. Blöch, *Phys. Rev. B* **50**, 17953 (1994).
- [28] J. P. Perdew, electronic structure of solids (Akademie Verlag, Berlin, 1991).
- [29] H. J. Monkhorst, and J. D. Pack, *Phys. Rev. B* **13**, 5188 (1976).
- [30] Y. Zeldovich, and Y. Raizer, *Physics of Shock Waves and High-Temperature Hydrodynamic Phenomena* (Academic Press, New York, 1966).
- [31] R. Kubo, *J. Phys. Soc. Jpn.* **12**, 570 (1957).
- [32] D. A. Greenwood, *Proc. Phys. Soc. London* **715**, 585 (1958).

- [33] A. F. Ioffe, and A. R. Regel, *Prog. Semicond.* **4**, 239 (1960).
- [34] N. F. Mott, 2nd edn. London, UK: Taylor and Francis.
- [35] W. J. Nellis, R. Chan, P. P. Edwards, and R. Winter, *Z. Phys. Chem.* **217**, 795 (2003).
- [36] W. J. Nellis, *J. Phys. Condens. Matter* **16**, S923 (2004).
- [37] W. J. Nellis, A. C. Mitchell, P. C. McCandless, D. J. Erskine, and S. T. Weir, *Phys. Rev. Lett.* **68**, 2937 (1992).
- [38] B. Holst, R. Redmer, and M. P. Desjarlais, *Phys. Rev. B* **77**, 184201 (2008).
- [39] G. W. Collins, L. B. Dasilva, P. Celliers, D. M. Gold, M. E. Foord, R. J. Wallace, A. Ng, S. V. Weber, K. S. Budil, and R. Cauble, *Science* **281**, 1178 (1998).